



Construction of carbon dots modified MoO₃/g-C₃N₄ Z-scheme photocatalyst with enhanced visible-light photocatalytic activity for the degradation of tetracycline

Zhijie Xie, Yiping Feng*, Fengliang Wang, Danni Chen, Qianxin Zhang, Yongqin Zeng, Wenying Lv, Guoguang Liu*

Institute of Environmental Health and Pollution Control, School of Environmental Science and Engineering, Guangdong University of Technology, Guangzhou, Guangdong 510006, China



ARTICLE INFO

Keywords:

Carbon quantum dots
g-C₃N₄
MoO₃
Z-scheme
Visible light photocatalysis

ABSTRACT

Carbon quantum dots (CDs) have been frequently used for broadening spectrum light response due to their superior up-conversion photoluminescence (UPPL) property and effective charge separation capacity. In this study, a novel CDs modified Z-scheme photocatalyst (CDs/g-C₃N₄/MoO₃) was successfully constructed. The morphologies, chemical compositions, and optical properties of the prepared catalysts were investigated via a series of characterization techniques. Systematic studies indicated that the CDs/g-C₃N₄/MoO₃ photocatalyst exhibited remarkably enhanced visible-light photocatalytic activity for the degradation of tetracycline (TC) compared to pristine g-C₃N₄ and MoO₃/g-C₃N₄ composite. Doping 0.5% CDs resulted in the highest TC degradation rate, which was 3.5 and 46.2 times higher than that of MoO₃/g-C₃N₄ and g-C₃N₄, respectively. The enhanced photocatalytic performance of CDs/g-C₃N₄/MoO₃ can be attributed to the synergistic effects of CD properties (i.e., excellent UPPL activity and high charge separation capacity and the Z-scheme heterojunction structure). Reactive species scavenging experiments revealed that photogenerated holes are the main active species during the photocatalytic process. Possible photocatalytic degradation pathways of TC were proposed through the identification of intermediates using HPLC-MS and the frontier electron density calculation. Experimental results showed that the newly fabricated Z-scheme CDs/g-C₃N₄/MoO₃ is a promising photocatalyst for the removal of TC from the environment.

1. Introduction

In the past decades, tetracycline (TC) has been widely used to treat human and animal infections [1]. It has been frequently detected in various environmental matrices. The presence of TC in the environment could cause antibiotic resistance problem, which poses a serious threat to the well-being of human and animals. However, due to the stable chemical structure and recalcitrance to biological degradations, TC cannot be effectively removed through conventional wastewater treatment processes [2,3]. Therefore, new techniques for the treatment of TC in wastewater are required. Recent years, photocatalytic degradation of TC from wastewater has received a lot of attention due to its high efficiency and long-term reliability. Some of traditional photocatalysts, e.g., TiO₂ [4], have been proven to have the ability to degrade TC under UV light irradiation. However, the poor utilization of solar light energy of these photocatalysts hindered their practical application. Therefore, the sunlight -driven photocatalysts are needed for the photocatalytic

treatment of TC.

Graphitic carbon nitride (g-C₃N₄) as a new visible light-driven photocatalyst has attracted enormous attention due to its low toxicity, high stability, and low cost [5]. As a metal-free polymeric semiconductor, g-C₃N₄ has a narrow band gap of ca. 2.7 eV and thus has a strong visible-light response. This property results in electrons and holes easily produced under visible-light excitation [6]. However, the high recombination rate of the photogenerated electron-hole pairs and the low specific area of pure g-C₃N₄ greatly limited its photocatalytic activity [7,8]. Therefore, various methods have been developed to improve the photocatalytic performance of the pure g-C₃N₄, including nonmetal doping [9,10], metal deposition [11], coupling with other materials to form hybrids [12,13], and using nano-sized structures g-C₃N₄ [14,15]. In particular, combining g-C₃N₄ with other semiconductors to form the Z-scheme heterostructured photocatalyst would efficiently separate the photogenerated electrons and holes, thus enhance the photocatalytic activity of g-C₃N₄ under visible light.

* Corresponding authors.

E-mail addresses: ypfeng@gdt.edu.cn, 454628362@qq.com (Y. Feng), liugg615@163.com, 454628362@qq.com (G. Liu).

MoO_3 is a well-known p-type metal oxide semiconductor and has been considered to be a promising candidate to form the Z-scheme heterostructured photocatalyst due to its unique energetic and electrical properties [16]. It has been demonstrated that combining MoO_3 with other photocatalyst, such as TiO_2 [17], CdS [18], and polyimides [19], enabled the composites with the excellent photocatalytic activity through the hindering of charge recombination and improving of charge transfer processes. Recent studies also found that the combination of MoO_3 with $\text{g-C}_3\text{N}_4$ could form the Z-scheme photocatalyst with enhanced photocatalytic performance [16,20]. Because of the suitable band gaps between the two semiconductors, the photogenerated charge carrier can be effectively separated and hence generated more reactive species. Nevertheless, it is still needed to improve the visible light absorption of the composites to achieve their high photocatalytic activity in their practical applications.

Carbon quantum dots (CDs), as a new discovered carbon-based nanomaterial, displayed the excellent up-conversion photoluminescence feature, as well as the outstanding photoinduced electron transfer and reservoir properties, all of which enabled the photocatalysts to utilize the sunlight efficiently [21]. Due to these remarkable properties, CDs have been successfully integrated with many semiconductors to improve their photocatalytic activities by decreasing electron-hole recombination and broadening the photo-absorption region. Our former studies also found that CDs could effectively improve the photocatalytic performances of TiO_2 [22], BiPO_4 [23], and $\text{g-C}_3\text{N}_4$ [24] for the degradation of PPCPs in water. Therefore, we are motivated to rationally design the carbon dots modified $\text{MoO}_3/\text{g-C}_3\text{N}_4$ Z-scheme photocatalyst with enhanced visible-light photocatalytic activity for potential practical application.

In this study, we reported the facile fabrication of CDs/ $\text{g-C}_3\text{N}_4/\text{MoO}_3$ composites, which showed excellent visible-light photocatalytic performance compared to that of the pristine $\text{g-C}_3\text{N}_4$, MoO_3 , and $\text{g-C}_3\text{N}_4/\text{MoO}_3$ hybrids. The microstructures, morphologies, phases, and optical properties of the samples were investigated via a series of characterization. Tetracycline (TC), as one of the most widely used antibiotics, was used to evaluate the photocatalytic activities of the prepared composites. The influences of MoO_3 and CDs contents on the photocatalytic performance of the CDs/ $\text{g-C}_3\text{N}_4/\text{MoO}_3$ composite were systematically evaluated. Electron spin resonance (ESR) and the reactive species trapping experiments were conducted to qualitatively detect the roles of the different active species during TC degradation. Subsequently, possible photocatalytic transformation pathway and mechanisms for TC degradation were proposed. Finally, the reduction of antibacterial activity of TC during the photocatalytic process was evaluated.

2. Experimental section

2.1. Catalyst preparation

All reagents (Taitan Company, China) employed for catalyst preparation were analytical grade and used without further purification. Deionized (DI) water from a Milli-Q apparatus ($> 18 \text{ m}\Omega \text{ cm}$, Germany) was used. MoO_3 powder was synthesized through the solid-state decomposition reaction of $(\text{NH}_4)_6\text{Mo}_7\text{O}_{24} \cdot 4\text{H}_2\text{O}$ at 500°C for 4 h in ambient air condition. The obtained product was then washed with DI water three times and dried at 60°C for 5 h.

Graphitic carbon nitride ($\text{g-C}_3\text{N}_4$) was synthesized by directly heating dicyandiamide [24]. Typically, 3.0 g of dicyandiamide was introduced into a covered alumina crucible, and then heated to 550°C for 3 h at a heating rate of $2.8^\circ\text{C min}^{-1}$. After cooling to room temperature, the obtained bulk $\text{g-C}_3\text{N}_4$ was milled into powders.

Carbon dots (CDs) were prepared by a hydrothermal method [24,25]. Briefly, citric acid (3.0 g) and urea (1.0 g) were dissolved in DI water by ultrasound for 2 h. The mixture was then transferred into a 50 mL Teflon-lined stainless steel autoclave at 180°C for 5 h. After

cooling to room temperature, the obtained black solution was centrifuged at 10,000 rpm for 30 min to remove large particles. Finally, the supernatant was collected and reconstituted to 100 mL with DI water for storage.

CDs/ $\text{g-C}_3\text{N}_4/\text{MoO}_3$ composite was synthesized through a facile calcination method [26]. In a typical procedure, 1.97 g of $\text{g-C}_3\text{N}_4$ and predetermined amounts of carbon dots and MoO_3 were co-dispersed in 50 mL ethanol through ultrasound for 2 h. The mixture was then carefully vaporized at 75°C by magnetic stirring to remove ethanol and was subsequently dried at 100°C for 12 h. The obtained powder was ground and then calcined at 300°C for 4 h in a muffle furnace. After cooling to room temperature, the product of interest was obtained. For comparison, a series of $\text{MoO}_3/\text{g-C}_3\text{N}_4$ composites with different mass contents of MoO_3 were also prepared using the same method, which are named as $\text{g-C}_3\text{N}_4/\text{MoO}_3 \cdot x$ (CMx), where x represents the mass fractions of MoO_3 . As can be seen in Text S1 of the Supplementary Materials (SM), the $\text{g-C}_3\text{N}_4/\text{MoO}_3 \cdot 3$ with weight contents of 3% MoO_3 has the highest photocatalytic activity. Thus, a series of CDs/ $\text{g-C}_3\text{N}_4/\text{MoO}_3$ composites with different mass contents of CDs were prepared and named as $y\text{-CDs/g-C}_3\text{N}_4/\text{MoO}_3 \cdot 3$ (yCCM3), where y represents the mass fractions of CDs.

2.2. Characterization

The microstructures of the synthesized catalyst were observed by a JSM-6700 scanning electron microscope (SEM) and a JEM-2100HR transmission electron microscope (TEM). The elemental compositions of samples were characterized by an energy dispersive spectroscopy (EDS) equipped on the SEM. X-ray diffraction (XRD, Bruker-D8-Advanced X-ray diffractometer) with Cu K α radiation source was used to characterize the crystal structure of samples, with the scanned area of 20 from 10° to 80° . The chemical components and valence states of the catalyst were analyzed using X-ray photoelectron spectroscopy (XPS) on a Thermo VG ESCALAB 250 spectrometer with Al K α radiation as the excitation source. The Fourier transform infrared (FT-IR) spectra were recorded on a Nicolet 6700 spectrometer with the samples dispersed in KBr. The UV-vis spectra were measured by an UV2450 UV-vis spectrometer (Shimadzu) using the BaSO_4 powder as the reference. The photoluminescence (PL) emission spectra were measured by a Flouromax-4 fluorescence spectrophotometer. The electron spin resonance (ESR) acquired on a Bruker A200-9.5/12 spectrometer was used to detect the radical intermediates.

2.3. Photocatalytic performance tests

Photocatalytic performances of the synthesized catalysts were evaluated by the photocatalytic degradation of tetracycline (TC) under visible light. TC (98% purity) was purchased from TCI Reagent Co. Ltd. (Shanghai, China). Visible-light irradiation was achieved by a 350 W xenon lamp with a 420 nm cutoff filter. A water circulation system was used to maintain the temperature at 25°C . In each test, 30 mg of catalysts were firstly dispersed in 50 mL of 20 mg L^{-1} TC aqueous solution, and then the mixture was stirred in dark for 30 min to reach the adsorption-desorption equilibrium before the light irradiation. During the reaction process, 2 mL of suspension was collected at predetermined time intervals, and filtered through 0.22- μm Millipore filters to remove the catalysts. The residue TC in solution was analyzed by high performance liquid chromatography (HPLC). HPLC was performed on a Waters e2968 instrument equipped with a UV detector and a $4.6 \times 250 \text{ mm}$ Zorbax Eclipse XDB C18 reverse-phase column (Agilent, USA) at 25°C . The detection wavelength of the UV detector was 355 nm and the injection volume was 20 μL . The isocratic mobile phase was made up of 25% methanol and 75% water (with 0.2% formic acid) with a flow rate of 1.0 mL min^{-1} .

2.4. Electrochemical measurements

The photoelectrochemical measurements were performed on a CHI-660 electrochemical system (Shanghai, China) equipped with a conventional three-electrode electrochemical cell. The prepared CM3 and 0.5CCM3 catalysts on ITO were served as the working electrodes, while Platinum (Pt) wire and saturated calomel electrode (SCE) were used as the counter and the reference electrodes, respectively. A 450 nm LED lamp (9 W, Shenzhen lamplic co., LTD, China) was used for the light irradiation. The photocurrent was recorded in 0.1 M sodium sulfate solution (Na_2SO_4).

2.5. Identification of by-products

Photodegradation intermediates of TC were identified by the HPLC-MS system equipped with an Agilent 1100 series HPLC coupled to a 6410 triple quadrupole mass spectrometer (Agilent Technologies, USA). 20 mg L⁻¹ TC was prepared for degradation products identification. After being irradiated for 120 min, the reaction solution was collected and concentrated with solid phase extraction (SPE) prior to LC/MS characterization [27]. Detailed information of SPE and HPLC-MS was listed in the Text S2 of SM.

2.6. Antibacterial tests

The antibacterial activities of TC solutions after photocatalytic degradation were assessed using the colony forming unit (CFU) counting method [28]. Briefly, 2 mL of TC reaction solutions were obtained at the interval of 0, 60, and 180 min and then filtered through 0.22-μm Millipore filter to remove catalysts. 100 μL of the diluted *E. coli* suspension was transferred to the obtained 2 mL filtrate. Then, the mixture was uniformly dispersed on the agar plate. The agar plate was incubated at 37 °C for 24 h and the CFUs were enumerated.

3. Results and discussion

3.1. Characterization

3.1.1. Structure and morphology characterizations

The XRD pattern of pure g-C₃N₄, MoO₃, CM3 and 0.5CCM3 are displayed in Fig. 1. Two diffraction peaks of pure g-C₃N₄ are observed at 13.0° and 27.4°, respectively corresponding to the in-plane structural packing motif and interlayer stacking structure of aromatic segments, which can be perfectly indexed to (001) and (002) crystal planes of graphitic materials. Pure MoO₃ has the main peaks at 12.8°, 23.4°, 25.7°, 25.8°, 27.3°, and 39.0°, respectively relating to the (020), (110), (040), (120), (021), and (060) planes. This observation is in good agreement with the standard JCPDF 35-0609 [29]. The XRD pattern of the CM3 composite indicated the coexistence of MoO₃ and g-C₃N₄. However, this pattern is similar to that of pure g-C₃N₄ due to the low content of MoO₃ in the composite. 0.5CCM3 composite also exhibited

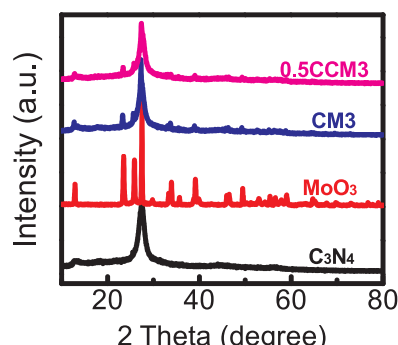


Fig. 1. XRD pattern spectra of MoO₃, g-C₃N₄, CM3 and 0.5CCM3 composite.

similar XRD patterns to that of CM3 composite, probably due to the low content of carbon quantum dots doping in the composite.

SEM images of the pure g-C₃N₄ and MoO₃, as well as 0.5CCM3 composite were shown in Fig. 2. Pure g-C₃N₄ displays lamellar-like and smooth morphology (Fig. 2a), while MoO₃ shows obvious edges and grain-like morphology (Fig. 2b). For the 0.5CCM3 composite, it is observed that the crystalline MoO₃ particles were wrapped in the thin amorphous g-C₃N₄ layers (Fig. 2c). Elemental mapping images in Fig. 2d showed that C, Mo, N, and O elements were well dispersed within the 0.5CCM3 matrix. The TEM images of 0.5CCM3 in Fig. 2e exhibited that MoO₃ was adhered to the g-C₃N₄ sheets with a grain-like morphology. From the high resolution TEM (HRTEM), it was clearly observed that CDs were distributed on the surface of the CM3 composites. In addition, the fringes with the interplanar spacing of ca. 0.21 and 0.35 nm were assigned to the (100) crystal plane of CDs and (040) crystal plane of MoO₃, respectively [29,30].

The surface compositions and chemical states of as-prepared CM3 and 0.5CCM3 catalysts were further examined using XPS. The XPS spectra of the as-prepared samples shown in Fig. 3a revealed that the existence of chemical elements Mo, C, N, and O on the surface of both CM3 and 0.5CCM3 catalysts. Because of the doping of CDs, the content of O on the surface of 0.5CCM3 catalyst is higher than that of CM3. The high-resolution XPS spectra of Mo3d, C1s, O1s, and N1s are shown in Fig. 3b-e. In CM3 sample, the Mo3d high resolution spectrum (Fig. 3b) showed two typical peaks at 233.1 and 236.3 eV. These peaks correspond to Mo3d^{5/2} and Mo3d^{3/2} for Mo⁶⁺ in MoO₃ [16]. However, for 0.5CCM3 composite, the characteristic peaks of Mo 3d^{5/2} and Mo 3d^{3/2} respectively shifted to 232.7 and 235.8 eV, which might be caused by the interactions among g-C₃N₄, MoO₃, and CDs. The high-resolution C1s spectrum (Fig. 3c) can be divided into four peaks at 284.8, 286.3, 287.3, and 288.1 eV. The C1s peaks at 286.3 and 287.3 eV are attributed to the C–O and C = O bonds, while the peak at 288.1 eV could be corresponded to the sp³-bonded C in C–N of g-C₃N₄, and the peak at 284.8 eV corresponded to C–C bond with sp² orbital or adventitious carbon [34]. Compared to the CM3, the C1s peak at 287.3 eV of 0.5CCM3 was significantly higher, which might be caused by the addition of CDs. The O1s XPS spectra in Fig. 3d were also comprised three main peaks at 530.7, 531.1, and 532.1 eV, corresponding to O²⁻ in molybdenum oxide, C=O, and C–OH, respectively [31]. Because of the presence of abundant carboxyl groups in CDs, the peak at 530.7 eV ascribed to C=O increased observably in 0.5CCM3 sample. The N1s XPS spectra peaks (Fig. 3e) of CM3 and 0.5CCM3 samples at 399.1, 400.7, and 401.6, 405.0 eV could be assigned to the triazine rings, N–(C) 3, N–H, and graphitic species, respectively [32,33].

The FTIR spectra of g-C₃N₄, MoO₃, CM3 and 0.5CCM3 samples are shown in Fig. 3f. The strong IR signals of pure g-C₃N₄ in the range of 1200–1631 cm⁻¹ are assigned to the typical C=N heterocycles and aromatic C–N stretching vibration modes, while the peaks at 808 and ~3200 cm⁻¹ are respectively related to the triazine units, and the stretching vibrations of N–H and C–OH [24,34,35]. For MoO₃, the peaks at 595 and 879 cm⁻¹ correspond to the oxygen linked among three metal atoms and Mo–O–Mo units, while the peak at 991 cm⁻¹ can be assigned to the Mo=O stretching mode [36]. Although the trace amount of MoO₃ has been added in CM3 and 0.5CCM3 catalysts, the characteristic peak of Mo=O was still easily found in these samples. Due to the C–O stretching vibrations [37], the characteristic peak at 1400 cm⁻¹ of 0.5CCM3 became stronger than CM3, indicating that the CDs have been successfully coated on the surface of CM3.

3.1.2. Optical and electrochemical properties

The optical absorption behaviors of g-C₃N₄, MoO₃, CM3, and 0.5CCM3 samples were investigated by UV-vis diffuse reflection spectra. As shown in Fig. 4a, the absorption edges of g-C₃N₄ and MoO₃ are at about 460 and 416 nm, which respectively agree well with their intrinsic band gaps of 2.7 and 3.0 eV [38]. The photocatalysts CM3 and 0.5CCM3 composites have absorption edges at about 485 and 515 nm

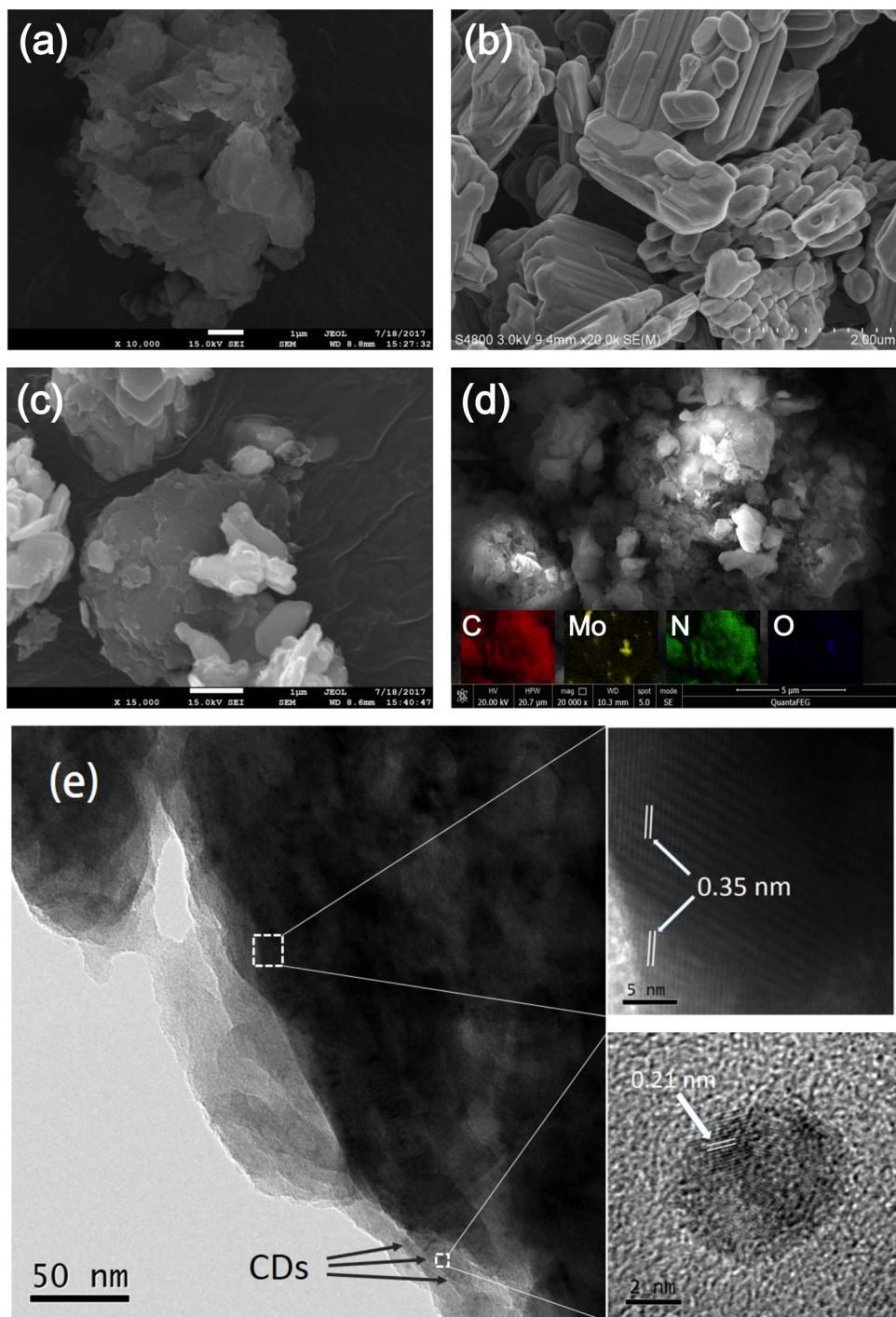


Fig. 2. SEM images of (a) C_3N_4 , (b) MoO_3 , (c) 0.5CCM3, (d) the elemental mapping of C, Mo, N, O elements in 0.5CCM3 composites, (e) TEM images of 0.5CCM3.

that corresponding to 2.55 and 2.40 eV, respectively. Compared to the pure $\text{g-C}_3\text{N}_4$ and MoO_3 , CM3 and 0.5CCM3 composites exhibited red-shift in the absorption edges. In addition, the absorption abilities of 0.5CCM3 in the visible light region enhanced significantly due to the presence of CDs [34]. The optical band gap of $\text{g-C}_3\text{N}_4$ and MoO_3 can be calculated according to the Eq. (1):

$$\alpha h\nu = A(h\nu - E_g)^{n/2} \quad (1)$$

where α , h , ν , E_g , and A are the absorption coefficient, Planck's constant, light frequency, band gap energy, and a constant, respectively. The n values of MoO_3 and $\text{g-C}_3\text{N}_4$ are 1 and 4, which are determined by the optical transition properties of a semiconductor [16,39]. As shown

in the inset Fig. 4a, the band gaps of MoO_3 and $\text{g-C}_3\text{N}_4$ were estimated to be 3.0 and 2.7 eV, which are in good agreement with the previous reported values [16,20].

The energy band structure of $\text{g-C}_3\text{N}_4$ and MoO_3 were determined via a Mott-Schottky plots and valence band X-ray photoelectron spectroscopy (VB-XPS) [40–42]. From Fig. S3, the positive slopes of curves show the typical n-type semiconductor characteristics of $\text{g-C}_3\text{N}_4$ [43,44]. The flat-band potentials of $\text{g-C}_3\text{N}_4$ were estimated to be -1.1 eV versus a saturated calomel electrode, and was determined to be -0.86 eV versus a normal hydrogen electrode. It is well known that the conduction band (CB) position of n-type semiconductor is 0.1–0.3 eV higher than of the flat-band potential [40]. Therefore, the

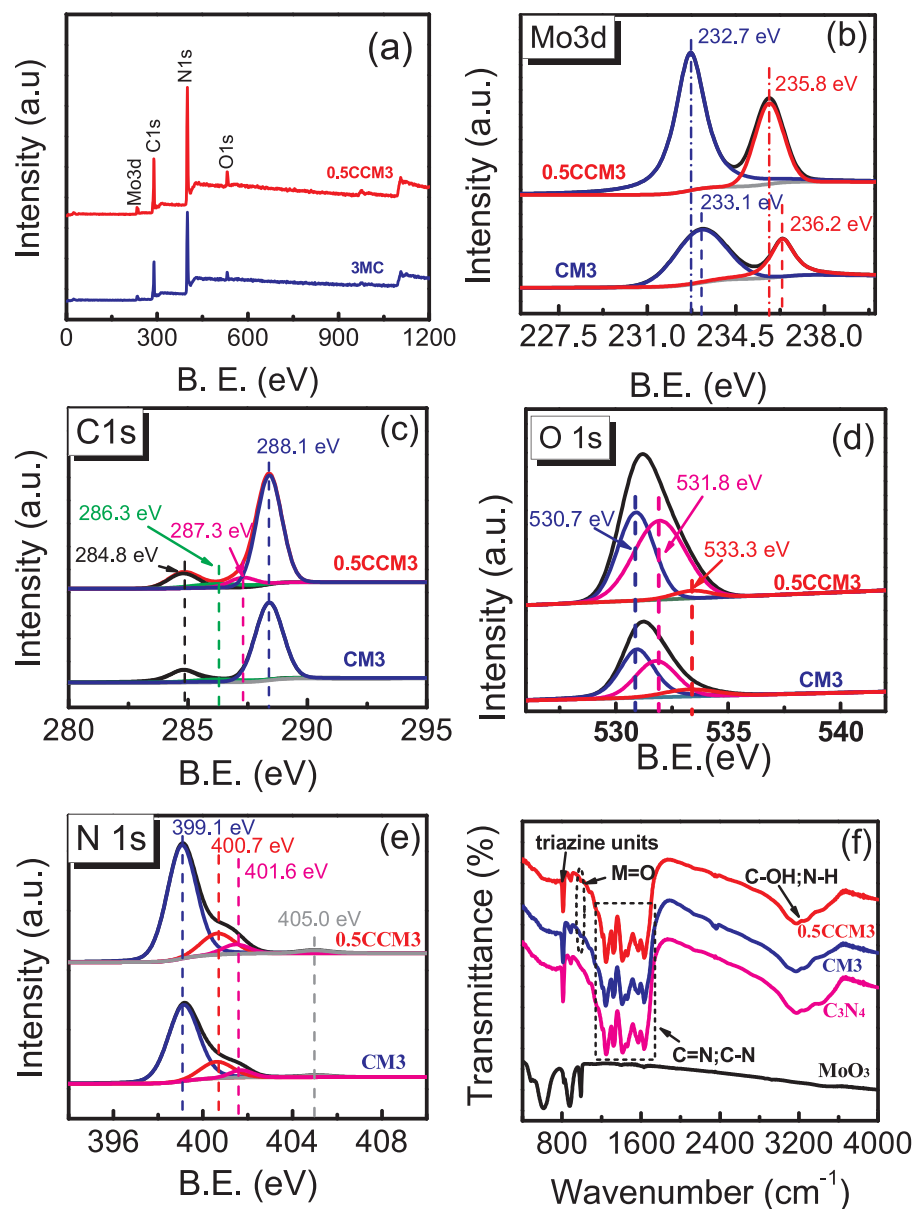


Fig. 3. (a) the full-scale XPS spectra of 0.5CCM3 and CM3 composites, high resolution XPS spectra of Mo3d (b), C1s (c), O1s (d), and N1s (e); (f) FTIR spectrum of MoO₃, g-C₃N₄, CM3, and 0.5CCM3.

CB of g-C₃N₄ was conjectured to be -1.16 eV. In addition, as shown in Fig. S3b, the valence band (VB) position of MoO₃ was estimated to be 3.54 eV through VB-XPS spectrum analysis. Hence, the VB positions of g-C₃N₄ was calculated as 1.54 eV, and the CB position of MoO₃ was determined to be 0.54 eV according to the empirical formula: $E_{VB} = E_{CB} + E_g$ [16,20].

PL analysis of pure C₃N₄, CM3, and 0.5CCM3 are shown in Fig. 4b. All these samples exhibited the emission peak at ca. 450 nm under an excitation wavelength of 300 nm [5,24]. After the loading of CDs, the PL intensity decreased remarkably, indicating that CDs efficiently improved the separation of photo-excited charge and holes [5,45]. The photocurrent response was then performed to further investigate the charge transfer behavior of the samples (Fig. 4c). It is obvious that the photocurrent density of 0.5CCM3 photocatalyst was about $1.5\text{--}2$ times higher than that of CM3, indicating that the lifetime of the photo-induced charge carriers of the 0.5CCM3 was effectively prolonged and hence enhanced the separation of electrons and holes, which was consistent well with PL analysis.

The band structure was shown in Fig. 4d. On the one hand, the

position of CB of MoO₃ (0.54 eV) was close to the VB position of g-C₃N₄ (1.53 eV), which made the mechanism of the Z-scheme system possible. On the other hand, the CB of g-C₃N₄ (-1.16 eV) was more negative than E_0 (O_2/O_2^{+} , -0.046 eV), hence the photogenerated electrons on the CB of g-C₃N₄ could react with oxygen to produce O_2^{+} [46]. Similarly, the VB of MoO₃ (3.54 eV) was positive than the potential of $\cdot OH/OH^-$ ($+2.27$ eV) [46,47], which the photogenerated holes are easy to oxidize OH^-/H_2O to product active species $\cdot OH$. It evidently shows that the CM follows the Z-scheme type mechanism to promote the separation of photogeneration electrons and holes, thus improves the photocatalytic efficiency.

Based on the above results, it can be concluded that CDs were successfully anchored onto the composites via the chemical bond interaction. This strong interaction might improve the transfer of photogenerated charge carriers and therefore reduced the recombination rate of the photoexcited electron-hole pairs. In addition, the superior optical of CDs might enhance the photo-absorbance and therefore facilitate the photocatalytic activity of 0.5CCM3.

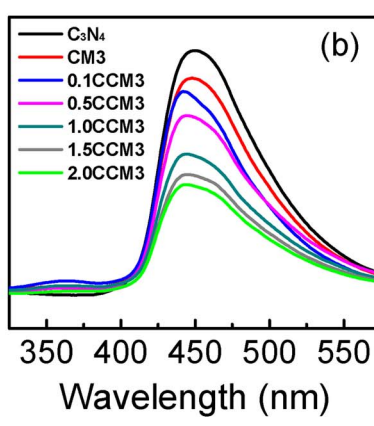
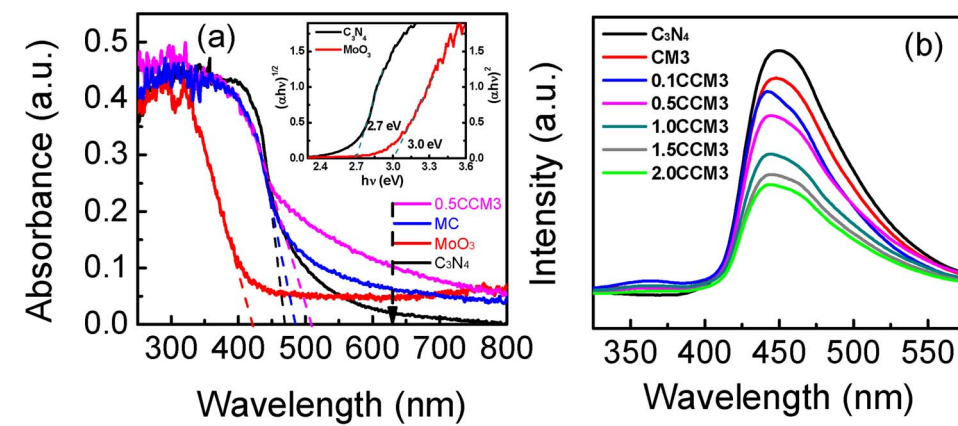


Fig. 4. (a) UV-vis diffuse reflectance absorbance spectra of MoO_3 , $\text{g-C}_3\text{N}_4$, CM3, and 0.5CCM3; (b) Photoluminescence (PL) emission spectra of $\text{g-C}_3\text{N}_4$, (1%–10%) $\text{MoO}_3/\text{C}_3\text{N}_4$ composites, and 0.5CCM3 with the excitation wavelength at 300 nm; (c) Photocurrent responses of CM3 and 0.5CCM3 composites which were excited by 450 nm LED light; (d) Band structures of $\text{g-C}_3\text{N}_4$ and MoO_3 .

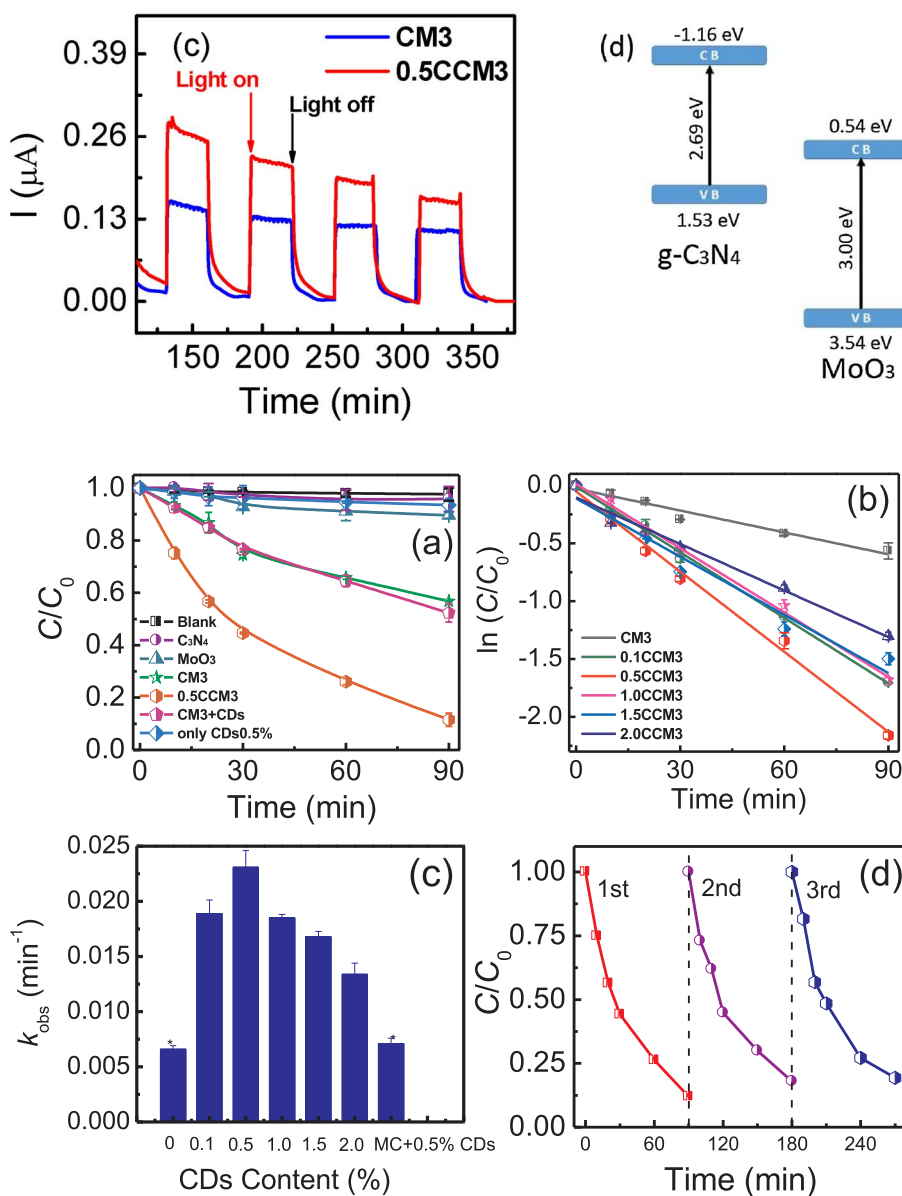


Fig. 5. (a) Photocatalytic activities of different photocatalysts based on the photocatalytic degradation of TC under visible light; (b) Kinetic rate constants of TC degradation over different contents of CDs; (c) The photocatalytic activities of the composites with different adding the content of CDs; (d) Photocatalytic degradation activities after three cycles of 0.5CCM3 photocatalyst under simulated visible-light irradiation.

3.2. Photocatalytic performance

The photocatalytic activities of the as-prepared samples were evaluated via the degradation of tetracycline (TC) under visible light irradiation. Without the presence of photocatalyst, TC concentration

change negligible within 90 min of visible light irradiation (Fig. 5a). In the presence of pure MoO_3 and $\text{g-C}_3\text{N}_4$, only ca. 10.1% and 5.3% of TC were decomposed within the same duration of visible light irradiation, respectively. In contrast, with $\text{MoO}_3/\text{g-C}_3\text{N}_4$ composite 43.2% of TC was removed in the same irradiation duration. However, the

Table 1

Scavengers used, RSs quenched and rate constants with quenched reactive species.

Quencher	RSs Quenched	K_{obs} (min ⁻¹)	Inhibition rate/%
Blank	\	0.0233	0
EDTA-2Na	h^+	0.0005	97.8
$\text{K}_2\text{Cr}_2\text{O}_7$	e^-	0.0191	18.0
IPA	$\cdot\text{OH}$	0.0176	24.4
BQ	$\text{O}_2^{\cdot-}$	0.0062	73.4
NaN_3	${}^1\text{O}_2$	0.0065	72.1

degradation of TC was remarkably improved after the loading of CDs. For example, the loading of a low content of CDs (0.5 wt %) resulted in 88.4% removal of TC. Nevertheless, experimental results also revealed that TC degradation efficiency highly depended on the loading of CDs. The photocatalytic activity of the CCM3 composites was increased from 0.0066 to 0.0231 min⁻¹ with the addition of CDs from 0 to 0.5%. However, further increase the CDs contents from 0.5% to 2.0% decreased the photocatalytic activity from 0.0231 to 0.0168 min⁻¹ (Fig. 5b–c). This phenomenon could be explained by inner filter effects that could compete for the photons required for the semiconductor at high CDs content [34].

To investigate the stability of the 0.5CCM3 photocatalysts, recycling experiment was conducted at the same conditions. As shown in Fig. 5d, after three recycling run, the TC photocatalytic degradation rate still remained at ca. 81.0%. In addition, no obvious structure change was observed after the photocatalytic reactions (Fig. S4), indicating the 0.5CCM3 composite exhibited the outstanding structural stability.

3.3. Photocatalytic mechanisms

Radical scavenging experiments were conducted to verify the roles of reactive species during the TC degradation. Ethylenediaminetetraacetate (EDTA-2Na, 1 mM), potassium dichromate ($\text{K}_2\text{Cr}_2\text{O}_7$, 50 μM), isopropanol (IPA, 10 mM), benzoquinone (BQ, 1 mM), and sodium azide (NaN_3 , 75 mM) were respectively applied as the trapping agent of h^+ , e^- , $\cdot\text{OH}$, $\text{O}_2^{\cdot-}$, and ${}^1\text{O}_2$ [48,49]. As shown in Table 1, the addition of $\text{K}_2\text{Cr}_2\text{O}_7$ and IPA resulted in the modest inhibition (< 25%) of the TC decomposition, while BQ, NaN_3 , and EDTA-2Na showed significant hindering effect on the decomposition of TC, in which inhibition rates increased to 73.4%, 72.1%, and 97.8%, respectively. The results indicated that h^+ played a vital role during the photocatalytic degradation of TC. To further confirm the existence of reactive oxygen species (ROS) during the photocatalytic process, ESR spin-trap spectra were carried with DMPO as the trapping agent. Obvious DMPO- $\text{O}_2^{\cdot-}$ signals and negligible signal of DMPO- $\cdot\text{OH}$ were observed over g-C₃N₄ under visible light irradiation (Fig. 6a–b). Comparing with the g-C₃N₄, both the DMPO- $\text{O}_2^{\cdot-}$ and DMPO- $\cdot\text{OH}$ signal intensities of CM3 composite were much higher than that of pure g-

C₃N₄. In addition, the existence of $\text{O}_2^{\cdot-}$ confirmed the formation of the Z-scheme heterojunction between MoO₃ and g-C₃N₄. Dramatically, the ESR signals of DMPO- $\text{O}_2^{\cdot-}$ and DMPO- $\cdot\text{OH}$ showed the significant enhancement after the introduction of CDs, indicating the promotion effect of CDs on the formation of RSs.

Based on the above results, a probable schematic mechanism was proposed. As shown in Scheme 1, due to the up-converted PL properties of CDs, light with wavelength > 460 nm could be converted into 350–650 nm light by CDs (Fig. S5). Then MoO₃ and g-C₃N₄ can efficiently absorb the up-converted UV and visible light with wavelength less than 416 nm and 460 nm, and hence the electron-hole pairs were photogenerated on the surface of MoO₃ and g-C₃N₄, respectively. In addition, owing to the Z-scheme heterojunction between MoO₃ and g-C₃N₄, photogenerated electrons in the CB of MoO₃ transferred quickly into the VB of g-C₃N₄ and recombined with the holes, leading to the accumulation of electrons in the CB of g-C₃N₄ and holes in the VB of MoO₃. Moreover, the accumulated electrons in the g-C₃N₄ could be further transferred and stored within carbon dots. Subsequently, the electrons could be trapped by O_2 to form superoxide radicals ($\text{O}_2^{\cdot-}$). Meanwhile, the holes in the VB of MoO₃ could oxidize OH-/H₂O to form $\cdot\text{OH}$ or take part in the organic pollutants degradation directly.

3.4. Products identification and theoretical calculations

LC-MS techniques were carried out to identify the intermediates of TC and the possible structures of the products that were elucidated based on the analysis of mass spectrum (Table S1). Products with m/z of 432.12 (P1), 416.12 (P2), and 395.10 (P4) were assigned as the dealkylation products of TC. The m/z 426.14 (P3) and 383.14 (P5) were identified as the dehydration products. Products with m/z 375.10 (P6), 363.13 (P7), 278.12 (P8), 337.12 (P9), 241.13 (P10), and 120.01 (P11) were assumed as the further oxidation products.

Frontier electron densities (FEDs) were calculated to predict the primary reactive sites for RSs attack [50]. The detailed information for the theoretical calculation was listed in Text S3 of SM. As shown in Table S2, the positions at N34, C19, C3, C27, C4, C2, and C6 showed higher FED_{HOMO} values, revealing that the photogenerate holes prefer to oxidize these positions. N34 and C19 also showed the higher FED_{HOMO} + FED_{LUMO} values, indicating that the N34 and C19 might be possibly attacked by ${}^1\text{O}_2$ and $\cdot\text{OH}$. In addition, C23 and C29 were easily attacked by $\text{O}_2^{\cdot-}$ due to their positive point charges [51].

On the basis of the degradation intermediates identification and reactive sites prediction, the potential photocatalytic degradation pathways of TC, including hydroxylation, dealkylation, and dehydration over 0.5CCM3 photocatalysts under visible light were proposed, as presented in Scheme 2 and Table S1. Briefly, the tetracycline molecular with m/z = 444.15 was firstly attacked by the $\cdot\text{OH}$ to form its hydroxylated product (m/z = 460.15), and this intermediate was then transformed to the compound P1 (m/z = 432.12) via the dealkylation.

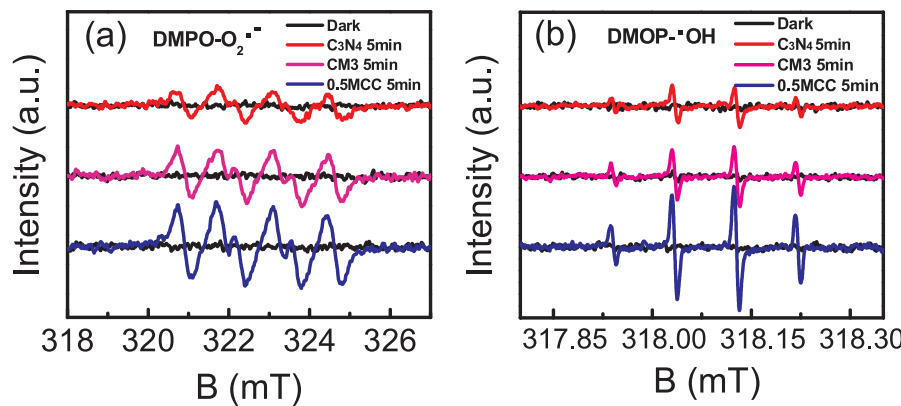
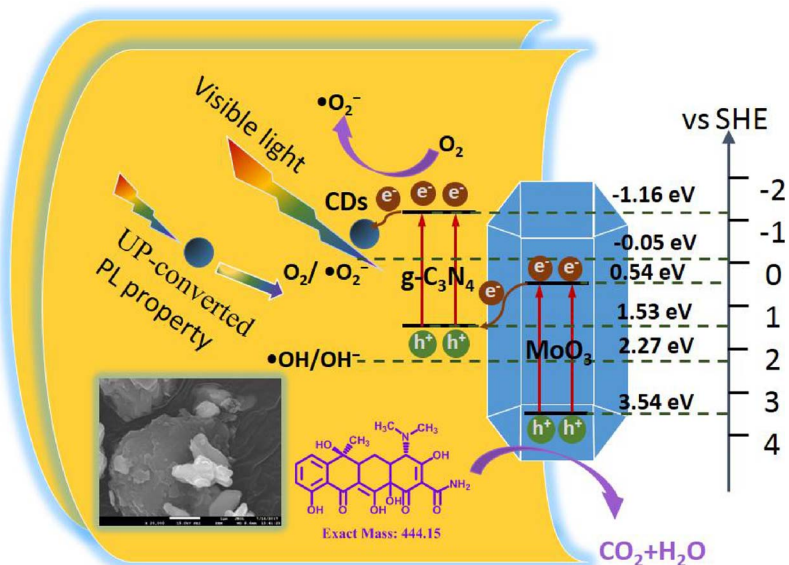
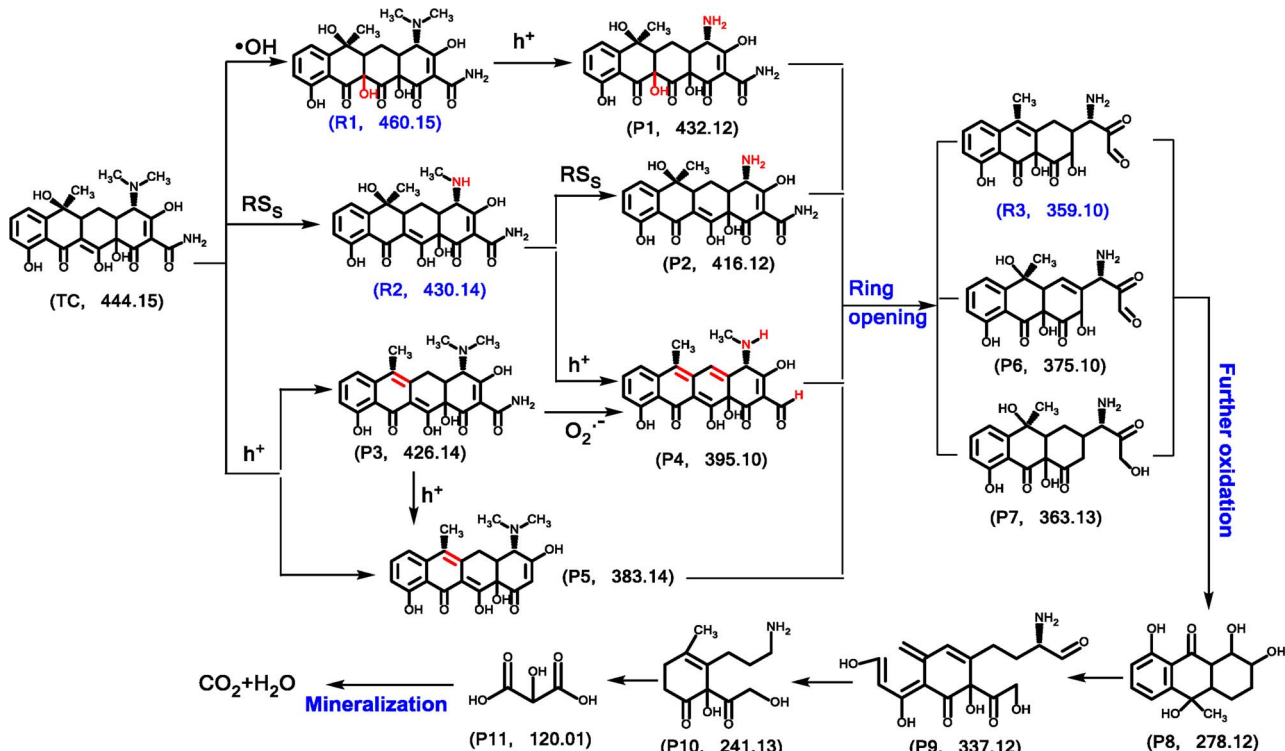


Fig. 6. ESR spectra of the (a) DMPO- $\text{O}_2^{\cdot-}$, and (b) DMPO- $\cdot\text{OH}$ adducts recorded with pristine g-C₃N₄, CM3, and 0.5CCM3 under visible light irradiation.



Scheme 1. Proposed photocatalytic degradation mechanisms of TC under visible light irradiation with 0.5CCM3 composites.



Scheme 2. The proposed transformation pathways of TC degradation.

Moreover, compound P4 ($m/z = 395.10$) and compound P5 ($m/z = 383.14$) were formed through dealkylation and dehydration reaction after the dehydration of the compound P3 ($m/z = 426.14$), respectively. The opening ring products including compounds P6 ($m/z = 375.10$), P7 ($m/z = 363.13$), P8 ($m/z = 278.12$), P9 ($m/z = 337.12$), P10 ($m/z = 241.13$), and P11 ($m/z = 120.01$) were formed through the further oxidation of products R3 ($m/z = 359.10$), P6 ($m/z = 375.10$) and P7 ($m/z = 363.13$). These ring-opening products were finally oxidized into CO_2 and H_2O .

3.5. Antibacterial tests

Fig. S6 showed the antibacterial activity change of the TC residue after photodegradation treatment. Clearly, due to the bacteriostatic effect of TC, the numbers of *E. coli* bacteria colonies were few (about 50 bacterial colonies) and the colonies were faintly seen with 20 mg L^{-1} TC before the light irradiation. In contrast, the number of colonies increased to ca. 100 and their size became bigger after 60 min photocatalytic reaction. After 180 min irradiation, hundreds of colonies covered on the whole culture medium, which was similar to the TC blank control. The above results revealed that the degradation intermediates arising from TC degradation had very low antibacterial

activity, which is promising for future application of 0.5CCM3 photocatalysts to remove TC and TC-related antibiotics from water.

4. Conclusions

In this study, we constructed a high-efficient Z-scheme CDs/g-C₃N₄/MoO₃ photocatalyst through a facile calcination method. The prepared 0.5CCM3 photocatalyst showed excellent photocatalytic properties on tetracycline degradation under visible light comparing with g-C₃N₄/MoO₃ and pristine g-C₃N₄. The analysis of reactive species confirmed that h⁺ played dominant role in the photocatalytic degradation of TC. CDs as electron reservoir enhanced the separation and optical converter, and hence improved the photocatalytic activity of g-C₃N₄/MoO₃ Z-scheme photocatalyst. In addition, the antimicrobial property of TC was decreased after the photodecomposition, indicating the great potential for practical application of CDs/g-C₃N₄/MoO₃ Z-scheme photocatalyst in further TC and TC-related antibiotics wastewater treatment.

Acknowledgments

This work was supported by the National Natural Science Foundation of China (21707019 and 21677040), the Innovative Team Program of High Education of Guangdong Province (2015KCXTD007), and the Science and Technology Planning Project of Guangdong Province (2017A050506052, 2017A020216010, and 2017B020216003).

Appendix A. Supplementary data

Supplementary material related to this article can be found, in the online version, at doi:<https://doi.org/10.1016/j.apcatb.2018.02.011>.

References

- [1] S. Leong, D. Li, K. Hapgood, X. Zhang, H. Wang, *Appl. Catal. B Environ.* 198 (2016) 224–233.
- [2] G.I. De, R. Muñoz, B. Guieysse, J. Hazard. Mater. 229–230 (2012) 446–449.
- [3] H. Kim, Y. Hong, J.E. Park, V.K. Sharma, S.I. Cho, *Chemosphere* 91 (2013) 888–894.
- [4] X.D. Zhu, Y.J. Wang, R.J. Sun, D.M. Zhou, *Chemosphere* 92 (2013) 925–932.
- [5] Q. Liu, Y. Guo, Z. Chen, Z. Zhang, X. Fang, *Appl. Catal. B Environ.* 183 (2016) 231–241.
- [6] Y. Su, P. Chen, F. Wang, Q. Zhang, T. Chen, Y. Wang, K. Yao, W. Lv, G. Liu, *RSC Adv.* 7 (2017) 34096–34103.
- [7] F. Dong, L. Wu, Y. Sun, M. Fu, Z. Wu, S.C. Lee, *J. Mater. Chem.* 21 (2011) 15171–15174.
- [8] S.C. Yan, Z.S. Li, Z.G. Zou, *Langmuir* 25 (2009) 10397–10401.
- [9] L. Ge, C. Han, *Appl. Catal. B Environ.* 117–118 (2012) 268–274.
- [10] J. Zhang, M. Zhang, G. Zhang, X. Wang, *ACS Catal.* 2 (2012) 940–948.
- [11] W. Zhao, G. Yang, S. Wang, H. He, C. Sun, S. Yang, *Appl. Catal. B Environ.* 165 (2015) 335–343.
- [12] L. Ge, C. Han, J. Liu, *Appl. Catal. B Environ.* 108 (2011) 100–107.
- [13] V. Vo, N.V. Kim, N.T.V. Nga, N.T. Trung, T.G. Le, P.V. Hanh, L.H. Hoang, S.J. Kim, *J. Electron. Mater.* 45 (2015) 1–7.
- [14] M. Zhang, J. Xu, R. Zong, Y. Zhu, *Appl. Catal. B Environ.* 147 (2014) 229–235.
- [15] S. Wang, C. Li, T. Wang, P. Zhang, A. Li, J. Gong, *J. Mater. Chem. A* 2 (2014) 2885–2890.
- [16] L. Huang, H. Xu, R. Zhang, X. Cheng, J. Xia, Y. Xu, H. Li, *Appl. Surf. Sci.* 283 (2013) 25–32.
- [17] F. Kong, L. Huang, L. Luo, S. Chu, Y. Wang, Z. Zou, *J. Nanosci. Nanotechnol.* 12 (2012) 1931–1937.
- [18] Z. Shen, G. Chen, Y. Yu, Q. Wang, C. Zhou, L. Hao, Y. Li, L. He, R. Mu, *J. Colloid Interface Sci.* 412 (2012) 31–38.
- [19] C. Ma, J. Zhou, H. Zhu, W. Yang, J. Liu, Y. Wang, Z. Zou, *ACS Appl. Mater. Interfaces* 7 (2015) 14628–14637.
- [20] Y. He, L. Zhang, X. Wang, Y. Wu, H. Lin, L. Zhao, W. Weng, H. Wan, M. Fan, *RSC Adv.* 4 (2014) 13610–13619.
- [21] H. Li, R. Liu, S. Lian, Y. Liu, H. Huang, Z. Kang, *Nanoscale* 5 (2013) 3289–3297.
- [22] P. Chen, F. Wang, Z.F. Chen, Q. Zhang, Y. Su, L. Shen, K. Yao, Y. Liu, Z. Cai, W. Lv, *Appl. Catal. B Environ.* 204 (2017) 250–259.
- [23] Q. Zhang, P. Chen, M. Zhuo, F. Wang, Y. Su, T. Chen, K. Yao, Z. Cai, W. Lv, G. Liu, *Appl. Catal. B Environ.* 221 (2018) 129–139.
- [24] F. Wang, P. Chen, Y. Feng, Z. Xie, Y. Liu, Y. Su, Q. Zhang, Y. Wang, K. Yao, W. Lv, *Appl. Catal. B Environ.* 207 (2017) 103–113.
- [25] S. Qu, X. Wang, Q. Lu, X. Liu, L. Wang, *Angew. Chem.* 51 (2012) 12215–12218.
- [26] A. Iwase, Y.H. Ng, Y. Ishiguro, A. Kudo, R. Amal, *J. Am. Chem. Soc.* 133 (2011) 11054–11057.
- [27] Y. Feng, Q. Song, W. LV, G. IIU, *Chemosphere* 189 (2017) 643–651.
- [28] L. Tang, K.J.T. Livi, K.L. Chen, *Environ. Sci. Technol. Lett.* 2 (2015) 59–65.
- [29] T.H. Chiang, H.C. Yeh, *Materials* 6 (2013) 4609–4625.
- [30] J. Liu, Y. Liu, N. Liu, Y. Han, X. Zhang, H. Huang, Y. Lifshitz, S.T. Lee, J. Zhong, Z. Kang, *Science* 347 (2015) 970–974.
- [31] Y. Chen, C. Lu, L. Xu, Y. Ma, W. Hou, J.J. Zhu, *CrystEngComm* 12 (2010) 3740–3747.
- [32] G. Li, X. Nie, J. Chen, Q. Jiang, T. An, P.K. Wong, H. Zhang, H. Zhao, H. Yamashita, *Water Res.* 86 (2015) 17–24.
- [33] A.P. Dementjev, A.D. Graaf, M.C.M.V.D. Sanden, K.I. Maslakov, A.V. Naumkin, A.A. Serov, *Diam. Relat. Mater.* 9 (2000) 1904–1907.
- [34] J. Pan, Y. Sheng, J. Zhang, J. Wei, P. Huang, X. Zhang, B. Feng, *J. Mater. Chem. A* 2 (2014) 18082–18086.
- [35] W.J. Ong, L.L. Tan, S.P. Chai, S.T. Yong, *Chem. Commun.* 51 (2015) 858–861.
- [36] H. Sinaina, J.H. Dong, J.S. Lee, A. Phruuangrat, S. Thongtem, T. Thongtem, *J. Alloys Compd.* 516 (2012) 172–178.
- [37] X. Yu, J. Liu, Y. Yu, S. Zuo, B. Li, *Carbon* 68 (2014) 718–724.
- [38] Y. Li, L. Huang, J. Xu, H. Xu, Y. Xu, J. Xia, H. Li, *Mater. Res. Bull.* 70 (2015) 500–505.
- [39] M. Dhanasankar, K.K. Purushothaman, G. Muralidharan, *Solid State Sci.* 12 (2010) 246–251.
- [40] C. Zeng, Y. Hu, Y. Guo, T. Zhang, F. Dong, X. Du, Y. Zhang, H. Huang, *Appl. Catal. B Environ.* 194 (2016) 62–73.
- [41] C. Liu, Y. Zhang, F. Dong, A.H. Reshak, L. Ye, N. Pinna, C. Zeng, T. Zhang, H. Huang, *Appl. Catal. B Environ.* 203 (2017) 465–474.
- [42] F. Wang, Y. Wang, Y. Feng, Y. Zeng, Z. Xie, Q. Zhang, Y. Su, P. Chen, Y. Liu, K. Yao, *Appl. Catal. B Environ.* 221 (2017) 510–520.
- [43] D.W. Zhao, X.W. Sun, C.Y. Jiang, A.K.K. Kyaw, *Appl. Phys. Lett.* 93 (2008) 083305–083305–083303.
- [44] J. Chen, S. Shen, P. Guo, M. Wang, P. Wu, X. Wang, L. Guo, *Appl. Catal. B Environ.* 152–153 (2014) 335–341.
- [45] H. Li, R. Liu, S. Lian, Y. Liu, H. Huang, Z. Kang, *Nanoscale* 5 (2013) 3289–3297.
- [46] H. Huang, Y. He, X. Li, M. Li, C. Zeng, F. Dong, X. Du, T. Zhang, Y. Zhang, *J. Mater. Chem. A* 3 (2015) 24547–24556.
- [47] A. Chithambaram, N.S. Sanjini, A.C. Bose, S. Velmathi, *Catal. Sci. Technol.* 3 (2013) 1405–1414.
- [48] Y. Tian, W. Li, C. Zhao, Y. Wang, B. Zhang, Q. Zhang, *Appl. Catal. B Environ.* (2017) 136–146.
- [49] B. Wang, J. Di, P. Zhang, J. Xia, S. Dai, H. Li, *Appl. Catal. B Environ.* 206 (2016) 127–135.
- [50] M. Carrier, C. Guillard, M. Besson, C. Bordes, H. Chermette, *J. Phys. Chem. A* 113 (2009) 6365–6374.
- [51] T. An, H. Yang, G. Li, W. Song, W.J. Cooper, X. Nie, *Appl. Catal. B Environ.* 94 (2010) 288–294.